Absorption spectrum (340–640 nm) of pure water.   I.   Photothermal measurements

Frank M. Sogandares and Edward S. Fry

We measured the absorption spectrum (340–640 nm) of the purest available water with photothermal deflection spectroscopy.   Our spectrum exhibits an absorption minimum in the blue region of the spectrum that is deeper than in most previously documented pure-water absorption studies.   We attribute this to exceptional sample purity and our technique's inherent freedom from scattering effects.   Because the absorption minimum is significantly lower, our spectrum displays high-order molecular resonance structure not observed in any previous absorption studies to our knowledge.   We find the minimum in the absorption spectrum of pure water is 0.0062 ± 0.0006 m^{-1} at 420 nm and 25 °C.   © 1997 Optical Society of America
  Key words: Photothermal, absorption, spectroscopy, water, seawater.

1.   Introduction

Water plays a significant role in energy exchange between the Earth and the Sun; solar radiation absorbed by the oceans and converted to heat heavily influences terrestrial climate.   No less significantly, water is a key ingredient to life on Earth, due in large part to its absorption coefficient, which has a dramatic, narrow transmission window in what we call the visible region of the spectrum.[1]   As frequency increases, the absorption coefficient starts dropping at $\approx 10^{14}$ Hz; after falling ≈ 8 decades to a minimum at $\approx 7 \times 10^{14}$ Hz (blue), it begins rising and increases by ≈ 10 decades at $\approx 5 \times 10^{15}$ Hz.   The enormous variation in the absorption coefficient occurs within less than 1 decade of frequency.   It is, for example, within this very narrow transmission window that chlorophyll has its absorption bands and animal eyes function.

  For ocean color studies, the spectral absorption of pure water provides vital input into the modeling of spectral reflectance.[2]   In other oceanographic applications, it provides a baseline for studies of diffuse

attenuation coefficients in the oceans and of the absorption by dissolved or suspended organic and biological materials.   In fact, it has an important role in many scientific disciplines, e.g., biology, chemistry, meteorology.   Consequently, it has been studied in the visible and near-visible regions of the electromagnetic spectrum by a large number of researchers with a variety of techniques.   There are several reviews that provide many pertinent references to the literature.[3–6]

  The difficulties with the absorption spectra in this database are the notable inconsistencies, probably caused by a combination of both experimental error and unknown sample purity.   The result is considerable uncertainty about the actual values of the absorption of the purest water and about which spectral data are most reliable.   For researchers in the field of ocean optics, these problems can affect attempts at closure between field measurements of apparent ocean optical quantities and their theoretical values based on the inherent optical properties, e.g., absorption.

  Traditionally, optical absorption coefficients of liquid samples have been measured with Bouguer's law by using transmission techniques that were corrected for scattering.   For a source of intensity I_0, the intensity I transmitted a distance z in a sample is given by

$$I = I_0 \exp[-c(\lambda)z], \qquad (1)$$

where $c(\lambda)$ is the total extinction coefficient.   In terms of the absorption coefficient $a(\lambda)$ and the total

scattering coefficient $b(\lambda)$, we can write $c(\lambda) = a(\lambda) + b(\lambda)$. Relations analogous to Eq. (1) are Beer's law expressed in terms of the concentration of solute in a solution, and Lambert's law, which describes relative transmission.[7] By measuring I, I_0, and z, it is straightforward to invert Eq. (1) and find the extinction $c(\lambda)$.

However, the determination of $a(\lambda)$ by correcting $c(\lambda)$ for scattering is difficult because of the requirement to determine $b(\lambda)$. The latter includes not only scattering caused by suspended particulate matter but also scattering caused by density fluctuations in a pure liquid.[8] As a practical matter, particulate-free samples are extremely difficult to prepare, but, even if one could prepare them and measure the absorption coefficient in transmission, it would still be necessary to correct the total extinction coefficient for the effects of pure-liquid scattering. In the present study, we avoid scattering corrections by directly measuring $a(\lambda)$ with a technique that is inherently insensitive to scattering.

In the infrared, the liquid-water absorption spectrum is driven by harmonics of the O–H vibrational modes whose fundamental frequencies are $\nu_1 = 3280$ cm^{-1} for the symmetric stretch, $\nu_2 = 1645$ cm^{-1} for the scissors mode, and $\nu_3 = 3490$ cm^{-1} for the antisymmetric stretch.[9] In the liquid phase, these features are significantly broadened and shifted by intermolecular interactions. Given that the values of ν_1, $2\nu_2$, and ν_3 are so similar, some higher-order resonance and combination band features will coalesce in the visible region because of these broadening mechanisms. Most liquid-water absorption spectra exhibit some of these broadened absorption features.

The resonance structure at harmonics of the O–H stretch frequencies can be clearly seen in the near-infrared (700–1000-nm) absorption spectra of distilled water obtained by Curcio and Petty with a transmission technique.[10] A number of the vibrational mode assignments for H_2O, HDO, and D_2O in this spectral range were later made with similar measurements.[9] By using a photoacoustic technique, Patel and Tam observed the fifth and sixth harmonics of the O–H stretch at 604 and 514 nm, respectively; they also determined an anharmonic formula for the nth harmonic absorption peak (or shoulder).[11,12]

For ocean optics research, the regions of greatest interest are the near ultraviolet, visible, and near infrared; of particular importance are the spectral regions in which photosynthetic materials are active. Four selected examples of data in this region are the following:

(1) Querry *et al.* used a split-pulse, transmission method with corrections for scattering.[13] Their data span the 418–640-nm range in ~2-nm increments and exhibit an absorption minimum at 460 nm.

(2) Realizing the scattering problems inherent in transmission measurements, Hass and Davisson demonstrated a calorimetric technique to measure the absorption at two points, 488 and 514 nm.[14]

(3) Likewise, Tam and Patel (T&P) used a scattering insensitive, laser photoacoustic technique over the ranges 445–545 and 570–700 nm in frequency increments of 100 cm^{-1}; these data exhibit an absorption minimum at 470 nm.[11] As with many transmission measurements, absolute calibration of their instrument was made at only one wavelength, 589.9 nm. It should also be noted that Bohren has obtained theoretical upper bounds on the absorption coefficient with elementary radiative transfer considerations and field measurements of the diffuse attenuation coefficient[15]; the data of T&P significantly exceeded these bounds in the blue.

(4) Smith and Baker (S&B) have compiled a best-estimate absorption spectrum for the ocean optics community based on their own research as well as previous research of others.[5] In the visible region, this spectrum is based largely on the data of Morel and Prieur.[16] In the blue spectral region, S&B show significantly lower absorption than T&P, and the broad minimum in their data is centered at ≈ 430 nm.

These four absorption spectra are typical of absorption spectra in the literature; they are shown in Fig. 1 with our present data. Several features of Fig. 1 are significant.

First, as wavelength decreases from the near infrared to the blue-green region, the broadened fourth-, fifth-, and sixth-harmonic combinations of the O–H stretch modes (ν_1 and ν_3) appear as shoulders in the spectrum at approximately 740, 600, and 520 nm, respectively. To our knowledge our data are the first to show shoulders that are due to the seventh and eighth harmonics at 455 and 405 nm.

Second, in the near-infrared region above 600 nm, all the measured absorption spectra are in general agreement. This is in part because these absorption coefficients are relatively large and easier to measure and in part because pure water scattering is small compared with absorption at these wavelengths.

Third, as the wavelength decreases below 550 nm, the disagreement between different spectra becomes more significant. Published absorption data in the 400–500-nm range vary by almost an order of magnitude. The dominant source of this disagreement is most likely the variability in sample purity used by the different investigators; samples were prepared and stored under a variety of conditions. Other important considerations in the 400–500-nm range are the following: (1) pure water has such a low absorption coefficient that its measurement is quite difficult, (2) contamination can easily dominate the water absorption, and (3) scattering can be a major source of error since absorption and scattering are comparable in this spectral region.[8]

Few studies have been made in the near-ultraviolet region below 400 nm. Transmission data in this region (corrected for scattering) suggest that the absorption increases rapidly with decreasing wavelength.[3,5] Contaminants that absorb ultraviolet light, such as organic pollutants and
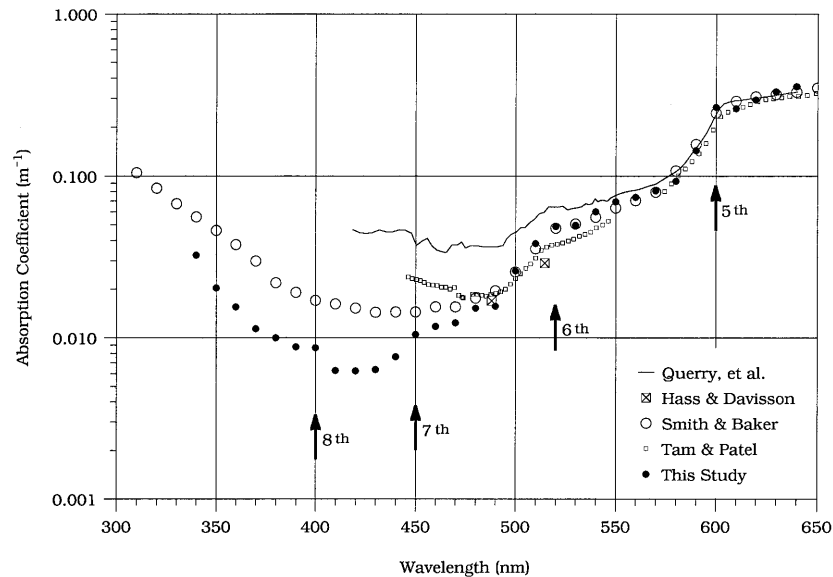
Fig. 1. Selected pure-water absorption spectra representative of variability in published data. Shoulders corresponding to harmonics of the O–H stretch are indicated by arrows.

dissolved gases, could significantly increase absorption in this region.

2. Photothermal Deflection Spectroscopy

A cross section illustrating the photothermal deflection spectroscopy (PDS) interaction is shown in Fig. 2. A high-power pulsed laser beam (the pump beam) produces a transient heat pulse in the interior of the absorbing sample; in analogy with our experiment, a cylinder lens focuses the pump beam in this illustration. A low-power, continuous-wave laser beam (the probe beam) propagates through this region of heating (the interaction region) at right angles to the pump beam and off center. The deflection of the probe beam by refraction in the dynamic temperature–index gradient is proportional to the absorption coefficient.

In a PDS experiment, only radiation that is absorbed and promptly converted to thermal energy
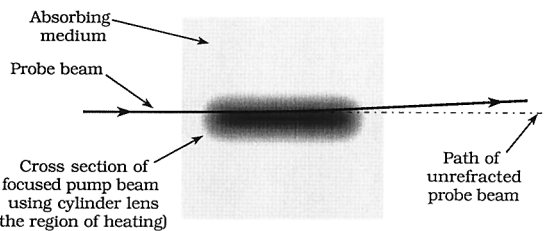
Fig. 2. In PDS a continuous-wave laser beam (probe beam) propagates through a region locally heated by a pulsed laser (pump beam). The probe beam is refracted (deflected) by the index gradient produced by local heating and is positioned to pass through a region of maximum gradient. The magnitude of the probe beam deflection depends linearly on the product aE, where a is the absorption coefficient and E is the energy in the pump beam pulse. In our experiment, the pump beam is focused with a cylinder lens and produces a locally heated cross section that is ≈ 5 mm long at the focal point.

deflects the probe beam; thus the absorption coefficients we measure reflect only this specific absorption process. For pure-water measurements, these results are expected to be consistent with usual interpretations of the absorption coefficient, as has been discussed for optoacoustic spectroscopy.[11] We also observed no fluorescence, even at 340 nm (the first excited electronic state for water appears at ~275 nm). Net energy deposition in the sample by Brillouin and Raman scattering is assumed to have a negligible effect on the PDS signal; specifically, their volume scattering coefficients are small, and each scattered photon carries away only slightly more or less energy than the incident photon.

It should be noted that many absorbing materials only weakly channel absorbed energy into heat; instead, they convert absorbed energy into fluorescence, chemical bonds, internal rovibrational excitation, and dissociation. The interpretation of PDS absorption spectra for these materials requires knowledge of the branching ratio for decay into thermal channels.

Numerous applications and theoretical treatments of PDS are documented in the literature[17,18]; hence only a brief sketch of the theoretical analysis for the dynamic refraction mechanism is provided here. In the absence of any mass transport (convection) from the region of heating, one can find the laser-induced temperature profile $T(r, t)$ by solving the heat equation (conservation of energy equation)[19,20]

$$-D\nabla^2 T + \frac{\partial T}{\partial t} = \frac{\dot{q}}{\rho C_p},\qquad(2)$$

where ρ is the density of the medium, C_p is the heat capacity of the medium at constant pressure, $\dot{q}$ is the thermal energy deposited in the medium per unit

volume per unit time, and D is the thermal diffusivity given by

$$D = \frac{k}{\rho C_p}, \qquad (3)$$

where k is the thermal conductivity. For water at 20 °C, the constants are k = 0.597 J s^{-1} m^{-1} K^{-1}, ρ = 998.2 kg m^{-3}, and C_p = 4182 J K^{-1} kg^{-1}.[21] These values together with Eq. (3) give $D = 1.4 \times 10^{-7}$ m^2 s^{-1}.

In the heat equation, the time scale for thermal diffusion is given by $\tau_{\mathrm{diffusion}} \sim L^2/D$, where L is the characteristic length scale of the heat source. With a focused probe beam, length scales are of the order of 10^{-5} m, so $\tau_{\mathrm{diffusion}} \sim 0.001$ s. Conversion of light energy to thermal energy on a time scale much less than $\tau_{\mathrm{diffusion}}$ will be considered instantaneous.

We represent the temporal dependence of the pump-laser pulses with a Dirac delta function, $E\delta(t - t_0)$, where E is the pump pulse energy. The transverse spatial dependence of the pump intensity (energy per unit time per unit projected area) is also assumed to have a Gaussian profile with a focused beam radius ω_0. The combined spatial and temporal dependence gives

$$I(r, t) = E\delta(t - t_0) \frac{2}{\pi\omega_0^2} \exp\left(\frac{-2r^2}{\omega_0^2}\right), \qquad (4)$$

where the constant factor ensures that the total integrated intensity gives the laser pulse energy E.

Consider an absorbing layer of thickness Δz (z is the pump beam propagation direction). In the present experiment, the pump and probe beams were chosen to be orthogonal; thus a relevant thickness Δz is the diameter of the probe beam. For a weakly absorbing medium $a\Delta z \ll 1$, and the reduction in the intensity $I(r, t)$ after traversing a thickness Δz is approximately $a\Delta z I(r, t)$, the intensity reduction per unit thickness $aI(r, t)$ is therefore constant across the probe beam diameter. We assume that all the light energy absorbed by the medium is converted instantly to heat, so $aI(r, t)$ is the thermal energy deposited in the medium per unit volume per unit time:

$$\dot{q} = aI(r, t) = \frac{2aE\delta(t - t_0)}{\pi\omega_0^2} \exp\left(\frac{-2r^2}{\omega_0^2}\right). \qquad (5)$$

Solving Eq. (2) in cylindrical coordinates with Eq. (5) in the source term gives the time dependence of the temperature at a distance r from the axis

$$T(r, t) = \frac{2aE\Theta(t - t_0)}{\pi\rho C_p[\omega_0^2 + 8D(t - t_0)]}$$
$$\times \exp\left[\frac{-2r^2}{\omega_0^2 + 8D(t - t_0)}\right], \qquad (6)$$

where $\Theta(t - t_0)$ is the Heaviside unit step function.

The path of the probe beam through an optical medium is described by the ray equation[22,23]

$$\frac{d}{ds}[\hat{\mathbf{s}}n(r, t)] = \nabla n(r, t), \qquad (7)$$

where $n(r, t)$ is the index of refraction, $\hat{\mathbf{s}}$ is a unit vector tangent to the ray path, and ds is an infinitesimal ray path element. Clearly, the path followed by a ray through the interaction region is determined by the refractive-index gradient. We determine this gradient based on the temperature dependence of the refractive index. The x and y Cartesian components of the gradient of the refractive index (gradients in the z direction are negligible) follow the form

$$\frac{\partial n}{\partial x_i} = \frac{\partial n}{\partial T} \frac{\partial T}{\partial r} \frac{\partial r}{\partial x_i} = \frac{x_i}{r} \frac{\partial n}{\partial T} \frac{\partial T}{\partial r}. \qquad (8)$$

By using Eq. (6) to determine $\partial T/\partial r$, we find

$$\frac{\partial n(r, t)}{\partial x_i} = -\frac{\partial n}{\partial T} \frac{8x_i aE\Theta(t - t_0)}{\pi\rho C_p[\omega_0^2 + 8D(t - t_0)]^2}$$
$$\times \exp\left[\frac{-2r^2}{\omega_0^2 + 8D(t - t_0)}\right]. \qquad (9)$$

Since the excess temperature generated in the interaction region is very small ($\Delta T \ll 0.1$ K), $\partial n/\partial T$ is constant during the measurement. By using an empirical equation for $n(T)$,[24] we find $\partial n/\partial T \approx 1 \times 10^{-4}$ °C^{-1} for pure water at 20 °C throughout the visible.

From Eq. (9), the peak photothermal response (maximum probe beam deflection) exhibits two important characteristics. First, the peak depends linearly on the absorption coefficient a and the pump pulse energy E; second, the peak occurs at $t = t_0$, i.e., when the pump laser fires.

To summarize, the experimental requirements are as follows:

(a) All samples must have low-absorption coefficients; a linear response in absorption requires $a\Delta z \ll 1$. Since the photothermal response of a pure-water sample is calibrated to the photothermal response of a reference sample of known absorption, the reference sample must also have sufficiently small absorption a_{ref} to give a linear response, $a_{\mathrm{ref}}\Delta z \ll 1$. If the latter condition is not satisfied, the nonlinearity of the photothermal response makes the calibration unreliable. With a 20-μm-diameter probe beam focus, our instrument is linear to an absorption of approximately 10.0 m^{-1}. Calibration was always performed with samples whose absorption was <2.0 m^{-1}.

(b) There must be no significant convective heat transfer within the sample. Convective heat transfer caused by excessive heating in the interaction region distorts the smooth laser-induced temperature profile, often in an unpredictable way. The result can be significant pulse-to-pulse variations in the magnitude and temporal shape of the photothermal

response. In the present study, the thresholds at which convective effects appear for high-absorption samples are at pump energies greater than 30 mJ/pulse and pulse rates greater than 2 Hz. These thresholds increase as the sample absorption decreases. Our PDS absorption spectra were all measured at conditions significantly below these thresholds.

(c) The heat source must approximate a delta function time dependence. Based on the data for pure water and given the 25-ns pulse width of our pump laser, this requirement is satisfied.

(d) Nonlinearity of the PDS signal must be made negligible. Since the refractive-index gradient is proportional to the temperature gradient produced by the pump-laser intensity profile, the dominant effect on the response linearity is the shape and smoothness of the pump beam profile. Thus maintaining a stable, spatially smooth profile at the focus of the pump-laser beam is important. We used a diode detector array to monitor the pump beam spatial quality.

(e) Scattering in the sample should be relatively small. In principle, PDS signals are independent of scattering; in practice, scattering affects the photothermal response in two ways. First, scattering particles that also absorb can produce additional heating in the interaction region that masks the photothermal response of the pure sample. Second, high levels of scattering can defocus the pump beam and reduce the index gradient. Experimentally, we found that quartz powder in suspension had little effect on the photothermal response until the sample became visibly turbid.

3. Experimental Setup: photothermal deflection spectroscopy

A XeCl excimer pumped dye laser produces the pump beam that is directed through attenuators and beam-shaping optics into the photothermal spectrometer. Photothermal transients are digitized, processed, and stored in the computer each time the excimer laser fires. Details are provided in the following subsections.

A. Computer Controls

The entire photothermal spectrometer is computer controlled with LabVIEW II software running on a Macintosh II computer over a general-purpose interface bus. The computer controls an analog-to-digital (A/D) board manufactured by GW Instruments, a Tektronix 2430 transient digitizer, and a pulsed joulemeter. LabVIEW software triggers the laser and reads the photothermal and joulemeter time series data from the transient digitizer. Each raw photothermal waveform $S(\lambda, t)$ is normalized to both the pump pulse energy E and the probe beam intensity I_p. Physical constraints imposed by linearity conditions etc. require a pump pulse rate less than 2 Hz, but our computer and digitizer limit the pulse rate to ~1.0 Hz.

B. Pump Laser System

A Lambda Physik EMG301-MSC excimer laser with XeCl (output wavelength is 308 nm) is used to pump a grating tuned Lambda Physik FL-3002 dye laser oscillator/amplifier. The excimer laser operated reliably, producing ~250 mJ, 25-ns pulses at ~1 Hz (well below its capabilities).

The dyes used to cover the range 340–640 nm (without frequency doubling) varied widely in efficiency and lifetime; their usable regions of coverage are the following: p-Terphenyl (340–350 nm), DMQ (350–370 nm), QUI (370–390 nm), DPS (400–410 nm), Stilbene 1 (420–430 nm), Coumarin 440 (430–450 nm), Coumarin 460 (450–480 nm), Coumarin 500 (490–530 nm), Coumarin 540A (530–580 nm), Rhodamine 6G (590–600 nm), Rhodamine 610 (600–640 nm), and Rhodamine 640 (640–650 nm). Because characteristics of the dye laser output (especially beam quality) varied with dye temperature, both the amplifier and oscillator dye circulators were temperature stabilized at ~20 °C with a closed cycle water circulator. Since acoustic noise from the dye circulators was an appreciable fraction of the photothermal noise floor, each circulator was acoustically isolated by using enclosures of 1-in. (2.54-cm) acoustic barrier foam.[25] Our dye laser system used two independent sets of dye circulating equipment so that one could be operational while another was being maintained.

Damage to the dye cuvettes by the high-power ultraviolet XeCl pump laser beam led to reduced and variable beam quality. This was avoided by maintaining careful alignment, thorough dye cuvette cleansing, and spatially filtering both the dye oscillator and dye amplifier laser beams. The photothermal pump beam was never single mode, but, as a result of the spatial filtering, it had a smooth Gaussian-like spatial profile and fulfilled the requirement discussed in Section 2.

C. Photothermal Spectrometer

Figure 3 shows a schematic of the photothermal spectrometer. The photothermal pump beam passes through a beam-shaping telescope with a 100-μm-diameter diamond spatial filter.[26] Following the telescope, a wedge beam splitter directs a small fraction of the pulse energy into a joulemeter (Molectron J3-05) whose signal triggers the transient digitizer.

The 5-mm-diameter pump beam is focused into the sample cell with a cylindrical lens (5-cm focal length) to produce a 5-mm-long pump region parallel to the probe beam. A cylindrical lens gives lower pump pulse intensity at the cell window than does a spherical lens; thus higher pump beam energies can be used without fracturing the cell window or excessively heating the sample locally. The magnitude and sign of the photothermal deflection depends on the axial separation of the pump and probe beams. By fine tuning the vertical position of the cylindrical lens, the photothermal response is optimized for maximum deflection. For a linear photothermal re-
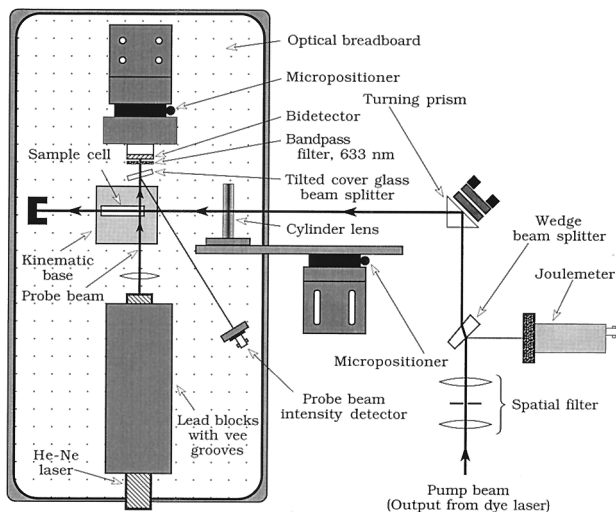
Fig. 3. Schematic of the photothermal spectrometer. Pump and probe intensities were measured with a pulsed joulemeter and a silicon photodiode, respectively. Axial separation of the beams was adjusted by moving the cylindrical lens up or down (in or out of the page) with the micropositioner.

sponse (normal operating conditions), the pump pulse energy E should be ≈ 1–20 mJ; appropriate neutral density filters can be inserted to reduce the dye laser output to these levels.

The probe laser, a Spectra Physics 102-3 He–Ne laser (1.5 mW), is focused into the sample cell and onto a silicon bidetector, FIL-S2DG,[27] on the opposite side of the cell. The probe beam deflection is proportional to the difference between the outputs of the two detector segments. Initially, the probe beam is centered so the same intensity is incident on each segment of the bidetector and the difference signal is zero. In this study, the bidetector had a sensitivity to probe beam deflections of ~ 125 mV μm^{-1}. Further details about bidetection of photothermal transients can be found in Jackson *et al.*[17] and in Sogandares.[28] Two points should, however, be emphasized. First, bidetection has an inherent factor

of 2 gain in signal over traditional intensity gradient detection. Second, the signal-to-noise ratio is independent of the distance between the interaction region and the detector, provided the probe beam is symmetric and entirely collected by the detector.

Figure 4 shows a schematic of the photothermal detection circuitry. The amplifier circuit consisted of a current-to-voltage converter followed by a simple voltage amplifier. Active and passive filters followed the final amplifier stage and provided two outputs: a dc coupled (low-pass filtered) output and an ac coupled (bandpass filtered) output. Since the photothermal detector is so sensitive to probe beam deflection, long time scale (of the order of 10 min) pointing errors can drive the detector output into saturation. To avoid this, we inverted the dc coupled output and fed it back into the motorized micropositioner circuit to keep the detector centered on the probe beam. This probe tracking circuitry can respond only to slow drifts in the probe beam position and will not track the transient photothermal deflection of the probe beam. The ac coupled output is the photothermal transient voltage and is recorded by a Tektronix 2430 transient digitizer.

We measured the probe beam intensity I_p by using a tilted cover glass to reflect a small fraction of the probe beam onto a large area silicon photodiode, PIN-10D.[27] This dc signal is amplified, digitized by a GW Instruments A/D board in the Macintosh II, and read by the LabVIEW program.

Resolution in PDS is strongly influenced by the pointing stability of the probe laser beam and by detector noise. The latter is due to noise from electrical and optical sources as well as from the acoustic noise coupled into the detector by way of the sample cell and detector mounts. Pointing stability is partially an inherent property of the laser and partially introduced by microphonics. One can minimize microphonics by mounting the cylindrical laser head between vee grooves in two lead blocks [2 in. (5 cm) $\times$ 4 in. (10 cm) $\times$ 8 in. (20 cm)]. The photothermal detector is mounted on a motorized micropositioner,
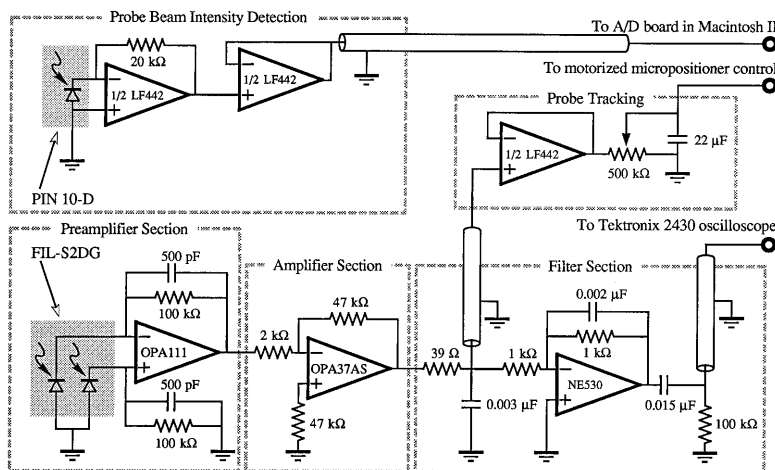

Fig. 4. Schematic of the detection electronics.

which is in turn mounted on a lead block to provide mechanical isolation between the table and the detector. The laser head, sample cell, and detector are all mounted on a Newport [12 in. (30 cm) × 24 in. (61 cm) × 2 in. (5 cm)] optical breadboard, which is placed on a 1-in. (2.54 cm) mat of acoustic barrier foam.[25] These efforts attenuated much of the microphonically coupled noise. Most of the microphonic noise remaining above 3 kHz was eliminated with two simple electronic filters at the detector output.

The excimer laser is the main source of electrical noise and generates electromagnetic interference at the leading edge of the photothermal transient. All circuit components are shielded from this by a metal enclosure and are powered by batteries within it. The primary source of optical interference is Rayleigh scattering of the pump beam into the detector by the sample. A He–Ne laser line interference filter at the entrance of the detector eliminates this noise at all pump wavelengths except 633 nm.

Our sample cell is a 4 cm × 4 cm × 1 cm quartz cell whose cover holds a temperature probe and sealed resistive heater. The cell is cemented to a 3-in. (8-cm) kinematic base and can be repeatedly removed and replaced in the same orientation. The probe beam is directed through the sample cell near the end window as shown in Fig. 3 for two reasons. First, since each photothermal transient is normalized to the pulse energy E, absorption of the pump beam between the window and the probe beam location reduces the effective incident pulse energy and produces a normalization error. For pure-water samples this is an insignificant error, but for the more highly absorbing calibration samples, the error could be significant. Making the path as short as possible minimizes the error. Second, external noise sources modulate the cell thickness and deflect the probe beam across the bidetector. In the frequency band of interest (~500–1000 Hz), the amplitude of the noise contributions at the edge of the cell is significantly smaller than at the center of the cell; of course, the edge of the cell is a node for vibrations of the cell wall. However, if the probe beam is closer than ~1–2 mm to the cell window, the shot-to-shot repeatability of the photothermal response deteriorates, probably as a result of thermal boundary effects on the interaction region. A probe–window separation of ~3 mm is used in this study.

The problems associated with maintaining a sample cell of ultrahigh cleanliness for the pure-water samples suggests the use of separate cells for calibration and pure-water samples. However, the experimental errors introduced by calibrating and correlating the photothermal responses of two different cells (which can never be identically oriented in the spectrometer) force us to use the same cell for both calibration and pure-water samples. High-purity water is a hungry substance,[29] making it an effective substance for cleaning the cell after a calibration solution has been used.

All calibration and pure-water samples were actively stabilized at 25.0(±0.1) °C with an off-the-shelf temperature controller and a quartz-sealed resistive heater. Recently, Pegau and Zaneveld[30] showed that the absorption spectrum in the near-infrared region has temperature-dependent components at the absorption shoulders produced by the fourth and fifth harmonics of the O–H stretch. However, for the fifth harmonic at 604 nm, this temperature dependence is only $\approx 0.6\%/°C$; the effect is even smaller at shorter wavelengths in the visible spectrum. Thus our temperature-stabilization procedure is sufficient to suppress any temperature variations in our absorption data.

D. Sample Quality and Preparation

Purity has been a major problem in previous experimental investigations of pure-water absorption, particularly in the blue and ultraviolet; pure-water samples were prepared by multiple distillation procedures and stored in a variety of ways. Our procedures attempt to address some of the previous shortcomings. Absolutely pure water is an unrealistic concept, so our pure water will simply be water that is as free from scattering particles and chemical contaminants as we are able to obtain. Ideally, any residual contamination is so small that the effect on our absorption measurements would be negligible; there will, unfortunately, be no direct proof of this.

High-purity water is corrosive and leaches absorbed contaminants and particulate bodies from nearly everything it touches. Researchers at Millipore Corp. have observed large increases in the concentration of metals in pure water that has been stored for 2 weeks under refrigeration in a Pyrex container, similarly, for the total organic carbon content of pure water stored in plastic.[29] From the standpoint of optical absorption, glass is better than Teflon or HDPE containers; we have observed that water stored in the latter has significantly higher absorption in the blue. Atmospheric gases and contaminants can also be absorbed at the air–water interface and increase the absorption, particularly in the ultraviolet. Pure-water samples must be measured before these effects can appreciably alter sample purity. In the present study, all pure-water samples are new, directly from the source as they are purified; none of the samples are older than ~30 min. All our containers are either Pyrex or quartz.

Our pure water is produced by commercially available instrumentation: a Millipore Milli-Q Ultrapure Ion/Organic-Free Water System that uses a variety of filters to polish the water. The system was modified by adding a deionization stage before the reverse osmosis filter, significantly extending the reverse osmosis filter lifetime; see the system schematic in Fig. 5. When properly serviced, this Millipore system routinely produces water of the highest quality (defined as the lowest absorption we have measured in the blue). Preparation of high-purity water samples that give consistently reproducible absorption data involves no more than running the instrument until the resistivity peaks (typically at ~18 MΩ cm), then

A) Chlorine prefilter
B) Deionization prefilter
C) Reverse osmosis filter
D) Storage tank
E) Carbon filter
F) Cation filter
G) Anion filter
H) Organic filter
J) 0.22-μm particle filter
K) Type II water outlet
   (resistivity > 1 MΩ-cm)
L) Type I water outlet
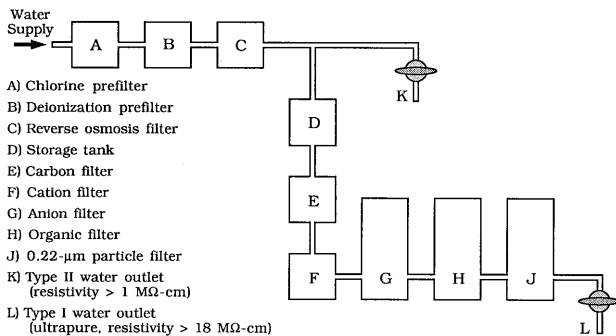   (ultrapure, resistivity > 18 MΩ-cm)

Fig. 5. Schematic of the Millipore Milli-Q pure-water system. To minimize contamination, all pure-water samples were drawn from the Type I outlet (L) directly into the sample cell. Before each sample was drawn, the system was run until the resistivity peaked at ~18 MΩ cm; typically, ≈1/2 l of water was discarded prior to sample collection.

purging the first half liter and filling the photothermal sample cell directly from the high-purity outlet.

4. Calibration and Data Collection and Analysis

We prepared a high-absorption (~100-m^{-1}) calibration sample by dissolving a nonfluorescing textile dye, Irgalan Black (IrB)[31] in water, and filtering the solution through two submicrometer Millipore filters to remove fine undissolved particles. The absorption of this solution is then measured in a Cary 219 dual-beam spectrophotometer whose accuracy was verified to within 0.5% with a set of NIST liquid-absorption standards.[32] Highly absorbing calibration samples are necessary in order to minimize the instrumental uncertainties of the Cary; they are later diluted for calibration of the photothermal spectrometer.

An absorption spectrum for a sample of IrB is shown in Fig. 6 and illustrates the relatively uniform, gray nature of this absorbing dye. This contrasts with the absorption spectrum of potassium permanganate whose absorption contains resonance structures and varies by a factor >20 over the visible spectrum; when it was used to calibrate a photoacoustic spectrometer, calibration was only performed at a single wavelength.[11] However, as a result of wavelength dependencies in the instrumentation, e.g., focal properties of lenses, it is critical to
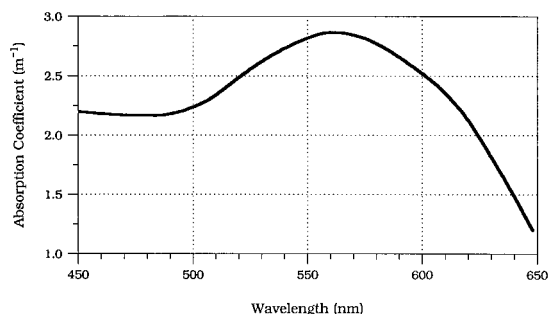

Fig. 6. Absorption spectrum of IrB.

calibrate throughout the spectrum; the gray nature of IrB greatly facilitates this calibration.

After precise dilution of the high-absorption IrB calibration sample to an absorption level required for PDS calibration ($\approx$1–2 m^{-1}), the sample has a total absorption coefficient $a(\lambda)_{\mathrm{sample}}$ given by

$$a(\lambda)_{\mathrm{sample}} = a(\lambda)_{\mathrm{IrB}} + a(\lambda)_{w}, \qquad (10)$$

where $a(\lambda)_{\mathrm{IrB}}$ is the known absorption coefficient of the IrB solute and $a(\lambda)_{w}$ is the absorption coefficient of pure water.

For each IrB calibration sample at each wavelength, n (generally, $n = 200$) photothermal transient waveforms S_i ($i = 1, \ldots, n$) are recorded. Each S_i consists of an array of 515 amplitude values at successive time intervals of 1/128 ms. Every S_i is normalized to its corresponding pump pulse energy E_i and probe intensity I_p, and the n normalized waveforms are averaged to give the calibration signal

$$S_c(\lambda, t) = \frac{1}{n} \frac{1}{I_p} \sum_{i=1}^{n} \frac{S_i}{E_i}. \qquad (11)$$

This signal S_c must be proportional to $a(\lambda)_{\mathrm{sample}}$:

$$S_c(t) = K(t)(a_{\mathrm{IrB}} + a_w) + (\mathrm{dc})_c, \qquad (12)$$

where the dependence on λ is not explicitly shown, $(\mathrm{dc})_c$ is an experimental dc voltage offset, and the proportionality constant $K(t)$ represents the temporal response of the instrumentation. For every measurement at every wavelength, we experimentally verified that the photothermal response is proportional to the absorption by measuring $S_c(\lambda, t)$ and determining $K(t)$ in Eq. (12) for at least three different calibration samples.

Similarly, the normalized signal S_w for a purewater measurement is given by normalizing and averaging n' (generally, $n' = 1000$) photothermal transient waveforms S_i':

$$S_w(\lambda, t) = \frac{1}{n'} \frac{1}{I_p'} \sum_{i=1}^{n'} \frac{S_i'}{E_i'}, \qquad (13)$$

where I_p' and E_i' are probe beam intensity and pump pulse energy, respectively. Acquiring data for a single pure-water measurement requires ~25 min. By using the same proportionality constant $K(t)$ introduced in Eq. (12), we can write

$$S_w(t) = K(t)a_w + (\mathrm{dc})_w. \qquad (14)$$

Combining Eqs. (12) and (14) gives

$$S_w(t) = \frac{a_w}{a_w + a_{\mathrm{IrB}}} S_c(t) + \mathrm{dc} \equiv mS_c(t) + \mathrm{dc}, \quad (15)$$

where dc is a dc offset voltage. The slope m in Eq. (15) is determined by a linear least-squares fit of the calibration waveform $S_c(t)$ to the 515 measured data points for $S_w(t)$. Figure 7 shows an example of an average photothermal response S_w in pure water and
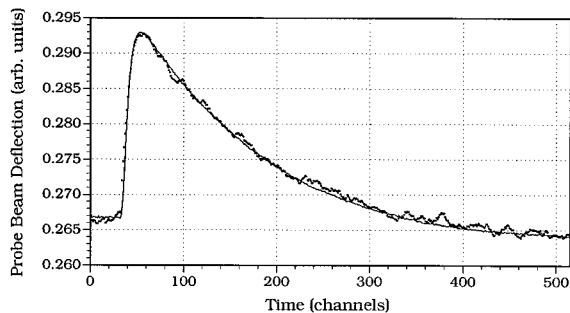
Fig. 7. Average of 1000 waveforms of the photothermal response in pure water together with the best fit of a reference waveform (λ = 500 nm). The reference waveform is a scaled calibration waveform that represents the instrument response under ideal noise conditions and provides the temporal response of the detector circuits. Each channel represents $1/128$ ms.

Fig. 8. Example of two calibration waveforms with slightly different time constants. The photothermal time constant depends on the pump–probe separation and changes slightly when the separation is adjusted. New calibration waveforms are required for the fit to each pure-water measurement.

the best fit of S_c. The pure-water absorption values are given by

$$a_w = \frac{m}{1-m} a_{\text{IrB}}. \tag{16}$$

For accurate calibration of the photothermal response, the pure-water absorption background should be significantly lower than the absorption of the IrB, $a(\lambda)_{\text{water}} \ll a(\lambda)_{\text{IrB}}$; i.e., $m \ll 1$. For our PDS calibration samples, $a(\lambda)_{\text{IrB}}$ was typically ~1–2 m^{-1}.

Each measurement at every wavelength is individually calibrated. After a wavelength change, the dye laser requires adjustments for beam quality and output power. The adjustments often change the output beam position and, consequently, the instrument calibration. Even when running for extended periods of time at a fixed wavelength, periodic beam maintenance, and hence recalibration, is required. The calibration is also made before and after every pure-water measurement; the pure-water waveform and the two calibration waveforms (from before and after) are all compared for matching temporal response. Occasionally, significant variations occur, indicating experimental changes that could lead to errors and require rejection of such data. Figure 8 shows an example of a typical variation that can be observed in calibration waveforms.

Since the detector is battery powered, its output slowly deteriorates. For fresh batteries, the differences in the before and after calibration responses are insignificant; however, if the decrease exceeds 1 or 2%, the batteries are replaced. Generally, the calibration responses are averaged.

The data collection and analysis procedure is summarized as follows: (a) the wavelength is set and laser parameters are optimized; (b) 200 photothermal calibration responses are recorded with an aqueous dye solution of known absorption; (c) the sample cell is thoroughly cleaned and then filled with high-purity water; (d) 1000 photothermal transients in high-purity water are observed, recorded, and averaged; (e) the instrument is recalibrated with the dye solution in order to check for instrumental drifts; (f) the
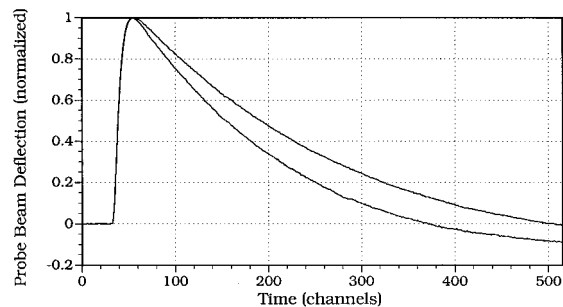
absorption coefficient is determined from a least-squares fit of the calibration response to averaged photothermal transient; (g) the wavelength is changed and steps a–f are repeated.

5. Data and Discussion

Our absorption data are shown in Table 1 and Fig. 1. We made the greatest number of measurements in the blue to violet spectral region and the fewest in the red and near ultraviolet. Measurements in the blue occasionally deviated widely from the average value; we believe these deviations are due to sample purity variations. Values quoted in Table 1 are averages of all but a few clearly inconsistent data points.

In the red, not only are absorption coefficients relatively large compared with those in the blue, but the effects of scattering are a less significant correction for transmission measurements. There is not a great deal of uncertainty in the red, and our data agree well with other data in this region.

However, below 500 nm, disagreement between the various absorption spectra becomes significant. Our data in this spectral region are significantly lower than the values quoted by S&B and exhibit additional resonance structure that is not clearly discernible in other measurements. Our data show absorption values below 0.01 m^{-1} from 380 to 450 nm with a minimum of 0.0062($\pm$0.0006) m^{-1} at 420 nm.

Below 400 nm, our spectrum exhibits a steep increase as wavelength decreases, but our absorption values are still consistently smaller than those of S&B. Contamination is a particularly severe problem in the blue and ultraviolet and has probably been an important factor in previous measurements. For example, at one wavelength, 350 nm, we were able to observe explicitly that the absorption of stored pure water increased significantly with time. To demonstrate this, a large sample of pure water was kept in a Pyrex flask and was used to refill the cell for each measurement. After six measurements, samples taken from the flask had been stored for 3 h. Increases from 4×10^{-3} to 7.5×10^{-3} m^{-1} h^{-1} were observed for the absorption coefficient at 350 nm, corresponding to increases of $\approx$20% to nearly 40%/h; however, we note that ob-

Table 1. Pure-Water Absorption Values Obtained in This Study[a]

Wavelength (nm)	Absorption Coefficient (m^{-1})	Uncertainty (m^{-1})	Error (%)
640	0.3560	0.0394	11
630	0.3310	0.0403	12
620	0.2950	0.0217	7
610	0.2610	0.0226	9
600	0.2660	0.0238	9
590	0.1440	0.0276	19
580	0.0933	0.0147	16
570	0.0813	0.0058	7
560	0.0741	0.0045	6
550	0.0697	0.0033	5
540	0.0604	0.0050	8
530	0.0498	0.0031	6
520	0.0488	0.0057	12
510	0.0384	0.0018	5
500	0.0260	0.0019	7
490	0.0157	0.0014	9
480	0.0153	0.0010	6
470	0.0124	0.0014	11
460	0.0118	0.0022	18
450	0.0105	0.0010	10
440	0.0076	0.0008	11
430	0.0064	0.0012	19
420	0.0062	0.0006	10
410	0.0063	0.0008	12
400	0.0087	0.0009	11
390	0.0088	0.0011	12
380	0.0100	0.0009	9
370	0.0114	0.0031	28
360	0.0156	0.0021	14
350	0.0204	0.0027	13
340	0.0325	0.0014	4

[a]All uncertainties include contributions from the calibration as well as from uncertainties in the linear fitting routine.

Table 2. Predicted and Observed Resonance Peaks[a]

Mode	Predicted Frequency (cm^{-1})	Predicted Wavelength (nm)	Observed Wavelength (nm)
5	16525	605	600
6	19452	514	520
7	22253	449	450
8	24928	401	400

[a]The predictions are based on an anharmonic form.[9,10] Since data were taken in 10-nm steps, the position resolution for each shoulder is limited to 10 nm.

served increases at 340 and 360 nm were still within statistical fluctuations. Nevertheless, as a result of these observations and to minimize the effect, we used freshly prepared water samples for each measurement at every wavelength. The data below 400 nm may still have a slight bias to the high side, although this bias is within quoted errors.

The locations of the resonance structures (shoulders in the absorption spectrum) can be characterized with the anharmonic formula obtained by Patel and Tam,[12] $v_n = n(3620 - 63n) \text{ cm}^{-1}$, where n is the mode

order. This relationship gives the approximate locations of harmonics listed in Table 2 and the corresponding shoulders are indicated by the arrows in Fig. 1. T&P observed the fifth and sixth harmonics[12]; to our knowledge our data appear to be the first to show the seventh and eighth harmonics. We believe these harmonics are observable because our water samples are very pure ($\sim$18-MΩ cm resistivity) and have lower absorption in the blue.

6. Summary and Conclusions

We have measured the spectral absorption of pure water from 340 to 640 nm with PDS, a technique that is relatively insensitive to scattering effects and is sensitive only to energy deposited in the sample in the form of thermal energy. Our spectrum is the first to show evidence of the seventh and eighth harmonics of the O–H stretch, and our absorption coefficients in the blue are significantly lower than those of previous investigators.

There are two important arguments in support of the lower absorption coefficients we observe in the blue. First, our commercial water purification system produced samples of a consistent and exceptional purity that has probably not been previously available. Second, our experience with deterioration of high-purity water samples during storage suggests such deterioration must have been a problem in many previous investigations.

References and Notes

1. J. D. Jackson, *Classical Electrodynamics*, 2nd ed. (Wiley, New York, 1975), pp. 290–292.
2. A. Morel, "Optical properties of oceanic case 1 waters, revisited," in *Ocean Optics XIII*, S. G. Ackleson and R. Frouin, eds, Proc. SPIE **2963,** 108–114 (1997).
3. H. Buiteveld, J. H. M. Hakvoort, and M. Donze, "The optical properties of pure water," in *Ocean Optics XII*, J. S. Jaffe, ed., Proc. SPIE **2258,** 174–183 (1994).
4. M. R. Querry, D. M. Wieliczka, and D. J. Segelstein, "Water (H_2O)," in *Handbook of Optical Constants of Solids II*, E. D. Palik, ed. (Academic, San Diego, Calif., 1991), pp. 1059–1077.
5. R. C. Smith and K. S. Baker, "Optical properties of the clearest natural waters (200–800 nm)," Appl. Opt. **20,** 177–184 (1981).
6. W. M. Irvine and J. B. Pollack, "Infrared optical properties of water and ice spheres," Icarus **8,** 324–360 (1968).
7. W. G. Driscoll and W. Vaughan (Eds.), *Handbook of Optics* (Optical Society of America, Washington, D.C., 1978), pp. 8-12–8-13.
8. A. Morel, "Optical properties of pure water and pure sea water," in *Optical Aspects of Oceanography*, N. G. Jerlov and E. S. Nielson, eds. (Academic, New York, 1974), pp. 1–24.

9. J. G. Bayly, V. B. Kartha, and W. H. Stevens, "The absorption spectra of liquid phase H_2O, HDO, and D_2O from 0.7 μm to 10 μm," Infrared Phys. **3,** 211–223 (1963).

10. J. A. Curcio and C. C. Petty, "The near infrared absorption spectrum of liquid water," J. Opt. Soc. Am. **41,** 302–304 (1951).

11. A. C. Tam and C. K. N. Patel, "Optical absorptions of light and heavy water by laser optoacoustic spectroscopy," Appl. Opt. **18,** 3348–3358 (1979).

12. C. K. N. Patel and A. C. Tam, "Optical absorption coefficients of water," Nature (London) **280,** 302–304 (1979).

13. M. R. Querry, P. G. Cary, and R. C. Waring, "Split-pulse laser method for measuring attenuation coefficients of transparent liquids: application to deionized filtered water in the visible region," Appl. Opt. **17,** 3587–3592 (1978).

14. M. Hass and J. W. Davisson, "Absorption coefficient of pure water at 488 and 541.5 nm by adiabatic laser calorimetry," J. Opt. Soc. Am. **67,** 622–624 (1977).

15. C. F. Bohren, "Absorption of pure water: new upper bounds between 400 and 580 nm," Appl. Opt. **23,** 2868 (1984).

16. A. Morel and L. Prieur, "Analysis of variations in ocean color," Limnol. Oceanogr. **22,** 709–722 (1977).

17. W. B. Jackson, N. M. Amer, A. C. Boccara, and D. Fournier, "Photothermal deflection spectroscopy and detection," Appl. Opt. **20,** 1333–1344 (1981).

18. J. A. Sell, "Optical ray tracing for crossed beam photothermal deflection spectroscopy," Appl. Opt. **26,** 336–342 (1987).

19. J.-M. Heritier, "Electrostrictive limit and focusing effects in pulsed photoacoustic detection," Opt. Commun. **44,** 267–272 (1983).

20. W. Nowacki, *Dynamic Problems of Thermoelasticity* (Noordhoff, Groningen, 1975).

21. R. C. Weast, M. J. Astle, and W. H. Beyer, eds., *CRC Handbook of Chemistry and Physics*, 68th ed. (CRC Press, Boca Raton, Fla., 1987), pp. F-10, D-171, and E-10.

22. K. D. Möller, *Optics* (University Science, Mill Valley, Calif., 1988).

23. M. Born and E. Wolf, *Principles of Optics*, 5th ed. (Pergamon, New York, 1975).

24. X. Quan and E. S. Fry, "An empirical expression for the index of refraction of seawater," Appl. Opt. **34,** 3477–3480 (1995).

25. The acoustic barrier foam was obtained from E•A•R Specialty Composites Corporation, Indianapolis, Indiana.

26. The diamond aperture is a wire die obtained from Fort Wayne Wire & Die, Fort Wayne, Indiana.

27. The PIN-10D photodiode was obtained from UDT Sensors, Inc., Hawthorne, California.

28. F. M. Sogandares, "The spectral absorption of pure water," Ph.D. dissertation (Texas A&M University, College Station, Tex., 1991).

29. "Ultrapure ion free/organic free water for trace analysis," Lit. No. CG302 (Millipore Corporation, Bedford, Mass., 1986).

30. W. S. Pegau and J. R. V. Zaneveld, "Temperature-dependent absorption of water in the red and near-infrared portions of the spectrum," Limnol. Oceanogr. **38,** 188–192 (1993).

31. Irgalan Black was obtained from CIBA-GEIGY Corporation, Greensboro, North Carolina.

32. The liquid absorption standards are identified by NBS#931d, Lot#680312 and were obtained from the NIST Office of Standard Reference Materials.